Supplementary Information

Huanyu Zhou,* Giuseppe Mallia and Nicholas M. Harrison

Department of Chemistry and Institute for Molecular Science and Engineering
Imperial College London, White City Campus, 80 Wood Lane, London, W12 0BZ, United Kingdom

**huanyu.zhou20@imperial.ac.uk*

S1 Computational and structural parameters

S1.1 Pseudopotentials

For consistency, PAW pseudopotentials based on the B86bPBE functional are generated for H, C, N and O with the 'ld1.x' program of QUANTUM ESPRESSO 7.1 [1,2]. All pseudopotentials are scalar relativistic. The non-linear core correction is used for C, N and O. Inputs are listed below.

H

```
&input
  title='H',
  zed=1.,
  rel=1,
  config='1s1 2p-2',
  iswitch=3,
  dft='b86bpbe'
/
&inputp
  lpaw=.true.,
  use_xsd=.FALSE.,
  pseudotype=3,
  file_pseudopw='H.b86bpbe-kjpaw_psl.UPF',
  lloc=1,
  which_augfun='PSQ',
  rmatch_augfun_nc=.true.,
  tm=.true.
/
3
1S  1  0  1.00  0.00  0.80  1.00  0.0
1S  1  0  0.00  0.05  0.80  1.00  0.0
2P  2  1 -1.00  0.05  0.75  0.75  0.0
```

C

```
&input
  title='C',
  zed=6.,
  rel=1,
  config='[He] 2s2 2p2',
  iswitch=3,
  dft='b86bpbe'
 /
&inputp
  lpaw = .true.,
  use_xsd=.FALSE.,
  pseudotype=3,
  file_pseudopw='C.b86bpbe-n-kjpaw_psl.UPF',
  lloc=-1,
  rcloc=0.9
  which_augfun='PSQ',
  rmatch_augfun_nc=.true.,
  nlcc=.true.,
  new_core_ps=.true.,
  rcore=0.7,
  tm=.true.
/
4
2S  1  0  2.00  0.00  1.00  1.20  0.0
2S  1  0  0.00  3.00  1.00  1.20  0.0
2P  2  1  2.00  0.00  0.90  1.40  0.0
2P  2  1  0.00  0.05  0.90  1.40  0.0
```

N

```
&input
  title='N',
  zed=7.,
```

```
  rel=1,
  config='[He] 2s2 2p3',
  iswitch=3,
  dft='b86bpbe'
/
&inputp
  lpaw = .true.,
  use_xsd=.FALSE.,
  pseudotype=3,
  file_pseudopw='N.b86bpbe-n-kjpaw_psl.UPF',
  lloc=-1,
  rcloc=1.2
  which_augfun='PSQ',
  rmatch_augfun_nc=.true.,
  nlcc=.true.,
  new_core_ps=.true.,
  rcore=0.7,
  tm=.true.
/
4
2S  1  0  2.00  0.00  1.00  1.30  0.0
2S  1  0  0.00  2.00  1.00  1.30  0.0
2P  2  1  3.00  0.00  0.90  1.35  0.0
2P  2  1  0.00  0.05  0.90  1.35  0.0
```

O

```
&input
  title='O',
  zed=8.,
  rel=1,
  config='[He] 2s2 2p4',
  iswitch=3,
  dft='b86bpbe'
/
&inputp
  lpaw = .true.,
  use_xsd=.FALSE.,
  pseudotype=3,
  file_pseudopw='O.b86bpbe-n-kjpaw_psl.UPF',
  lloc=-1,
  rcloc=1.1
  which_augfun='PSQ',
  rmatch_augfun_nc=.true.,
  nlcc=.true.,
  new_core_ps=.true.,
  rcore=0.7,
  tm=.true.
/
4
2S  1  0  2.00  0.00  1.00  1.30  0.0
2S  1  0  0.00  1.00  1.00  1.30  0.0
2P  2  1  4.00  0.00  0.90  1.35  0.0
2P  2  1  0.00  0.05  0.90  1.35  0.0
```

S1.2 DFT/ESM-RISM parameters

Slabs of the (001), (010), (011), (110) and (20$\bar{1}$) surfaces are modelled. Computational parameters are summarised in **Table S1**.

Table S1 Computational parameters of slabs

(*hkl*)	*k* grid	Relaxed molecules	Energy convergence threshold (Ry)	Laue-RISM starting point (Bohr)
(001)	2×2×1	8	2×10^{-5}	6.67
(010)	2×2×1	4	1×10^{-5}	12.22
(011)	1×2×1	8	2×10^{-5}	6.78
(110)	1×2×1	8	2×10^{-5}	9.60
(20$\bar{1}$)	2×1×1	8	2×10^{-5}	6.09

An example of the Laue-RISM input file is listed below.

```
&RISM
  nsolv               = 1
  closure             = 'kh'
  tempv               = 300.0
  solute_lj(1)        = 'opls-aa'
  solute_lj(2)        = 'opls-aa'
  solute_lj(3)        = 'opls-aa'
  solute_lj(4)        = 'opls-aa'
  rism3d_conv_level   = 0.3
```

```
  laue_expand_right    = 94.49
  laue_starting_right = <from Table S1>
/
SOLVENTS {g/cm^3}
  Eth     -1.0     Ethanol.oplsaa.MOL
```

The structure of the paracetamol solute used for ESM-RISM calculations is optimised by density functional theory as implemented in CRYSTAL23[3], using M06-2X/def2-TZVPPD. The default convergence thresholds of energy, force and displacement are used. Due to the lack of data, a very dilute solution is assumed, so the density of ethanol is used. The permittivity of paracetamol reported by McLoughlin *et al.*[4] is adopted. The OPLS-UA force field[5] that simplifies hydrocarbon H is used to parameterise the atomic charge and Lennard-Jones (LJ) potential. LJ parameters of hydroxyl H and amine H are modified according to the OPLS-UA model of ethanol by Nishihara[6] to address their artificial penetration into the bulk. The MOL file used is attached below. The inset below illustrates the labels of atoms.

```
<MOL version="1.0.0">
  <!--
    Copyright (C) 2023 Huanyu Zhou [spica.h.zhou@gmail.com]
  -->
  <MOL_INFO>
    Paracetamol for Ethanol solvent(OPLS-UA),
    whose geometry is calculated by M06-2X/def2-TZVPPD
    ------------------------------------------------------------------
    OPLS-UA parameters:
      W.L.Jorgensen et al., JACS, 1988, 110, 1657.
    Permittivity:
      C.M.McLoughlin et al., Powder Technol., 2003, 134, 40-51.
    Density:
      Use ethanol density - very dilute solution
    ------------------------------------------------------------------
  </MOL_INFO>
  <MOL_HEADER author="H.Zhou"
              date="05Mar2024"
              comment="Paracetamol"
              formula="C8H9NO2"
              has_charge="T"
              has_lj="T"
              number_of_atoms="13"/>
  <MOL_MASS type="real" size="1" columns="1" UNITS="g/mol">
    151.1626
  </MOL_MASS>
  <MOL_DENSITY type="real" size="1" columns="1" UNITS="g/cm^3">
    0.789
  </MOL_DENSITY>
  <MOL_PERMITTIVITY type="real" size="1" columns="1">
    8.4
  </MOL_PERMITTIVITY>
  <MOL_ELEMENT type="character" size="13" columns="1" len="7">
Oh/par
Oc/par
Ho/par
Hn/par
Coh/par
Ca/par
Ca/par
Ca/par
Ca/par
Ca/par
Co/par
Ch/par
N/par
  </MOL_ELEMENT>
  <MOL_XYZ type="real" size="39" columns="3" UNITS="angstrom">
     0.000000  0.000000  0.000000
     6.081967  2.327843 -0.020758
    -0.328225 -0.901746  0.007049
     5.979332 -0.803439 -0.007804
     1.363115  0.000000  0.000000
     2.011032  1.225888 -0.000490
     2.113864 -1.167603 -0.000492
     3.394774  1.299356 -0.002233
     3.496419 -1.098395 -0.003149
     4.152829  0.129030 -0.003698
     6.429902  1.167610 -0.015101
     7.893809  0.787468 -0.019447
     5.562863  0.111319 -0.005447
  </MOL_XYZ>
  <MOL_CHARGE type="real" size="13" columns="1">
    -0.700
    -0.500
    +0.435
    +0.300
    +0.265
    +0.000
    +0.000
```

```
    +0.000
    +0.000
    +0.000
    +0.500
    +0.000
    -0.300
  </MOL_CHARGE>
  <MOL_LJ>
    <MOL_EPSILON type="real" size="13" columns="1" UNITS="kcal/mol">
      0.170
      0.210
      0.046
      0.046
      0.110
      0.110
      0.110
      0.110
      0.110
      0.110
      0.105
      0.160
      0.170
    </MOL_EPSILON>
    <MOL_SIGMA type="real" size="13" columns="1" UNITS="angstrom">
      3.070
      2.960
      1.000
      1.000
      3.750
      3.750
      3.750
      3.750
      3.750
      3.750
      3.750
      3.910
      3.250
    </MOL_SIGMA>
  </MOL_LJ>
</MOL>
```

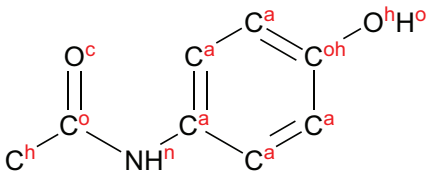

Due to the constrained computational resource, surfaces relaxed in pure ethanol are used. The structural change caused by paracetamol is believed to be negligible because of the assumed diluted solution. RISM control parameters are tuned for convergence, whose influences on the results are believed to be negligible. An exemplary input deck is attached.

```
&RISM
  nsolv               = 2
  closure             = 'kh'
  tempv               = 300.0
  solute_lj(1)        = 'opls-aa'
  solute_lj(2)        = 'opls-aa'
  solute_lj(3)        = 'opls-aa'
  solute_lj(4)        = 'opls-aa'
  mdiis1d_step        = 0.05
  rism3d_conv_level   = 0.3
  mdiis3d_step        = 0.1
  mdiis3d_size        = 20
  laue_expand_right   = 94.49
  laue_starting_right = <from Table S1>
/
SOLVENTS {g/cm^3}
  Eth     1.0     Ethanol.oplsaa.MOL
  Para     0.01   Paracetamol-Eth.oplsua.MOL
```

An explicit adsorption model consists of the surface relaxed in pure ethanol solution and a molecule relaxed with 3D-RISM. No structural relaxation is performed due to the limitation of computational resources. To reduce the dimension of unknowns, only translational movements of adsorbates along the z axis are considered, *i.e.*, the molecule is oriented as it is in the Form I crystal and is moved along the z axis only. The range of movement is defined as -0.5 Å to 5.0 Å away from the equilibrium adsorption site. Another constraint for the upper limit is that all atomic fractional coordinates of the adsorbate along the z axis should be less than 0.45 to reduce the influence of cell boundaries on the asymptotic behaviour of the RISM correlation functions (the lower and upper limits of DFT/ESM-RISM cell are -0.5 and 0.5, as required by QUANTUM ESPRESSO 7.1). The RISM solution consists of ethanol only since paracetamol has been explicitly

included.

The 'local-TF' mixing is used to improve the convergence of SCF calculations. The energy convergence criterion is set to 10^{-7} Ry to balance time consumption and accuracy. Other parameters are consistent with those reported in the **DFT/ESM-RISM calculation** section of the manuscript.

S1.3 Structural parameters

Structural parameters of the slabs used to model the (001), (010), (011), (110) and (20$\bar{1}$) surfaces are summarised in **Table S2**.

For all the slabs, the non-periodic direction is along the z axis vertical to the surface. The origin of the z axis is in the middle of the slab, as required by QUANTUM ESPRESSO 7.1[7]. All the z values reported in this work are commensurate with that.

Table S2 Structural parameters of slabs

(*hkl*)	Molecules	Layers	a (Å)	b (Å)	γ (Å)	Cross-sectional Area (Å^2)	z_1 (Å)	z_2 (Å)
(001)	12	3	9.03	12.77	90.00	115.30	6.50	11.55
(010)	8	4	11.78	7.00	81.33	81.58	6.53	11.96
(011)	12	3	12.77	11.43	104.53	141.24	3.26	9.44
(110)	12	3	14.85	7.00	83.13	103.22	5.63	12.96
(20$\bar{1}$)	12	3	9.03	14.59	90.00	131.73	5.80	9.60

S2 Wulff construction by experimental data

S2.1 Owens-Wendt method

Experimentally, contact angle measurement is used to probe the free energies of surfaces and interfaces, following the famous Young's equation[8]:

$$\cos\theta\,\gamma_{LV} = \gamma_{SV} - \gamma_{SL} - \pi_e \tag{S1}$$

θ is the contact angle between liquid and solid. γ_{LV},γ_{SV} and γ_{SL} are free energies of liquid and solid against their saturated vapor and of the solid-liquid interface. π_e is the equilibrium pressure, which is negligible when $\theta \geq 10^\circ$[9].

By the Owens-Wendt method[8], γ_{SV} and γ_{LV} consist of a dispersive component describing dispersion interactions and a polar component describing dipole-dipole interactions and hydrogen bonds. **Eq. S2** describes the relationship between contact angle and free energies.

$$(1+\cos\theta)\,\gamma_{LV} = 2\left(\sqrt{\gamma_S^d\gamma_L^d} + \sqrt{\gamma_S^p\gamma_L^p}\right) \tag{S2}$$

where $\gamma_{SV} = \gamma_S^d + \gamma_S^p$ and $\gamma_{LV} = \gamma_L^d + \gamma_L^p$. The superscript denotes dispersive (d) and polar (p) components.

Following **Eq. S2**, both the surface free energy and the polarizability of a substrate can be characterised by measuring its contact angles with two different liquid probes with known γ_L^d and γ_L^p. Similarly, the interface free energy γ_{SL} between liquid and substrate can be easily obtained if γ_S^d, γ_S^p, γ_L^d and γ_L^p are known[10]:

$$\gamma_{SL} = \gamma_{SV} + \gamma_{LV} - 2\left(\sqrt{\gamma_S^d\gamma_L^d} + \sqrt{\gamma_S^p\gamma_L^p}\right) \tag{S3}$$

As far as the authors are aware of, no measurement of contact angle between Form I paracetamol and ethanol has been reported. Heng *et al.*[11,12] measured γ_S^d and γ_S^p of (001), (010), (011), (110) and (20$\bar{1}$) surfaces of Form I paracetamol by contact angle measurement with water and diiodomethane as probes. Panzer[13] measured γ_L^d and γ_L^p of ethanol by contact angle and adsorption measurements of polymer. Data used and obtained in this work is summarised in **Table S3**.

Wulff construction

The morphology of Form I paracetamol is obtained by the Wulff construction that minimises interface free energies listed in **Table S3**. Compared to experimental and predicted morphologies (**Fig. 1**, manuscript), the morphology predicted by the Owens-Wendt method

Table S3 Free energies by Owens-Wendt method[11–13] (Unit: mJ/m^2)

System	γ^d	γ^p	γ
Ethanol	15.8	6.4	22.2
(001)	34.4	38.0	72.4
(010)	45.1	7.0	52.1
(011)	33.9	32.7	66.5
(110)	34.2	20.2	54.4
(20$\bar{1}$)	34.9	27.5	62.4
(001)/Ethanol			16.8
(010)/Ethanol			7.5
(011)/Ethanol		*Not applicable*	13.5
(110)/Ethanol			7.4
(20$\bar{1}$)/Ethanol			11.1

is elongated along the [001] axis, making the (001) facet absent. This is probably an overestimation of the effect observed by Ristic *et al.*[14], where the morphology is less dominated by the (001) facet as the supersaturation decreases. The appearance of (010) facet in **Fig. S1** illustrates that morphology prediction based on measured thermodynamic factors fails to reproduce the post-breakage growth behaviour of Form I paracetamol, in which case kinetic factors must be considered.

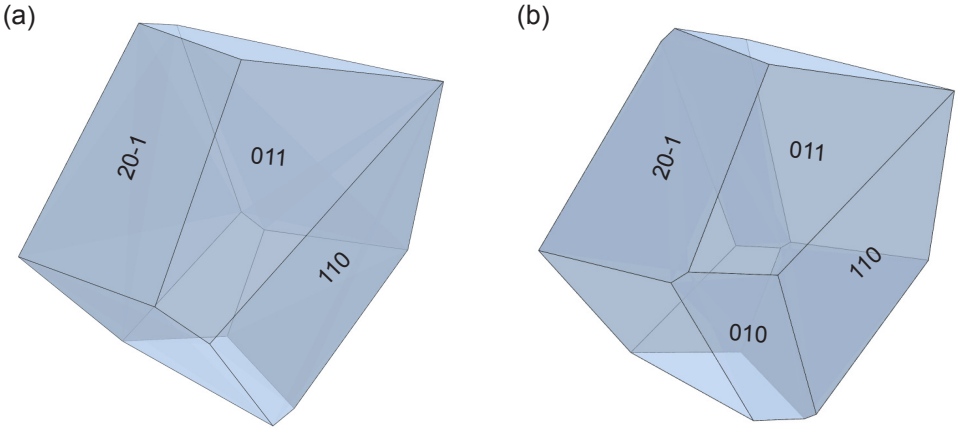

Fig. S1 Morphology of Form I paracetamol (a) without and (b) with the (010) facet.

S3 Supplementary figures and analysis

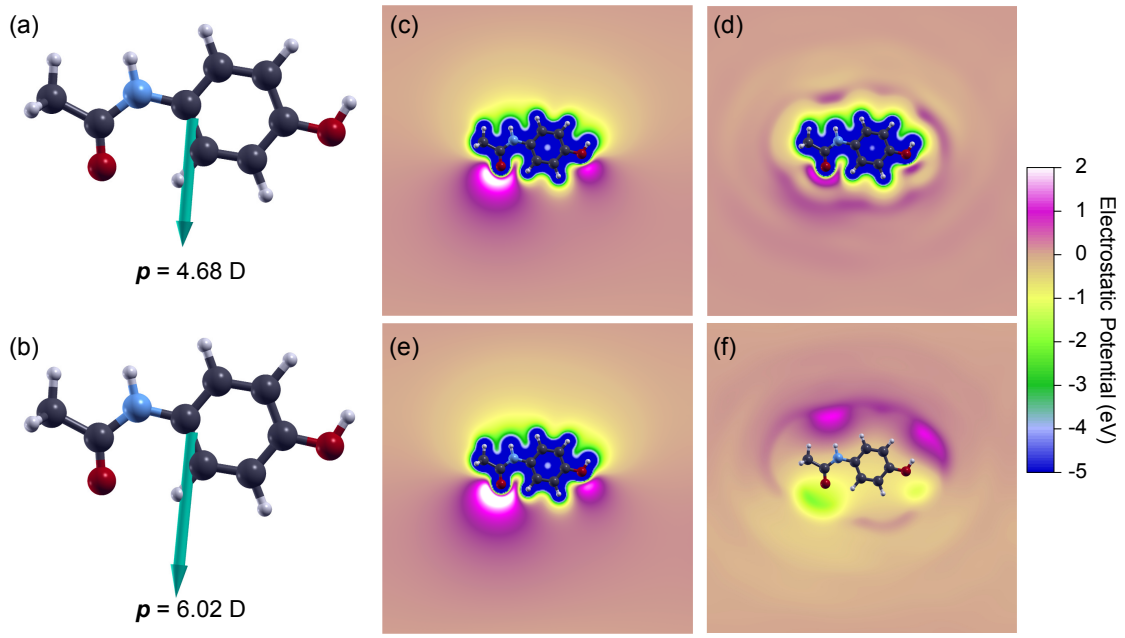

Fig. S2 Dipole moments of (a) gaseous and (b) solvated paracetamol molecules. The magnitude and orientation of dipole moments are indicated by green arrows pointing from the centre of mass of corresponding molecules. Electrostatic potentials of (c) gaseous paracetamol molecule, (d) paracetamol-ethanol solution, (e) paracetamol molecule as solute and (f) ethanol solvent.

To properly colour-code the regions of interest, the adopted colour scale in **Fig. S2** cannot correctly represent the potential field near covalent bonds (coloured in blue), whose magnitude is much lower than -5 eV.

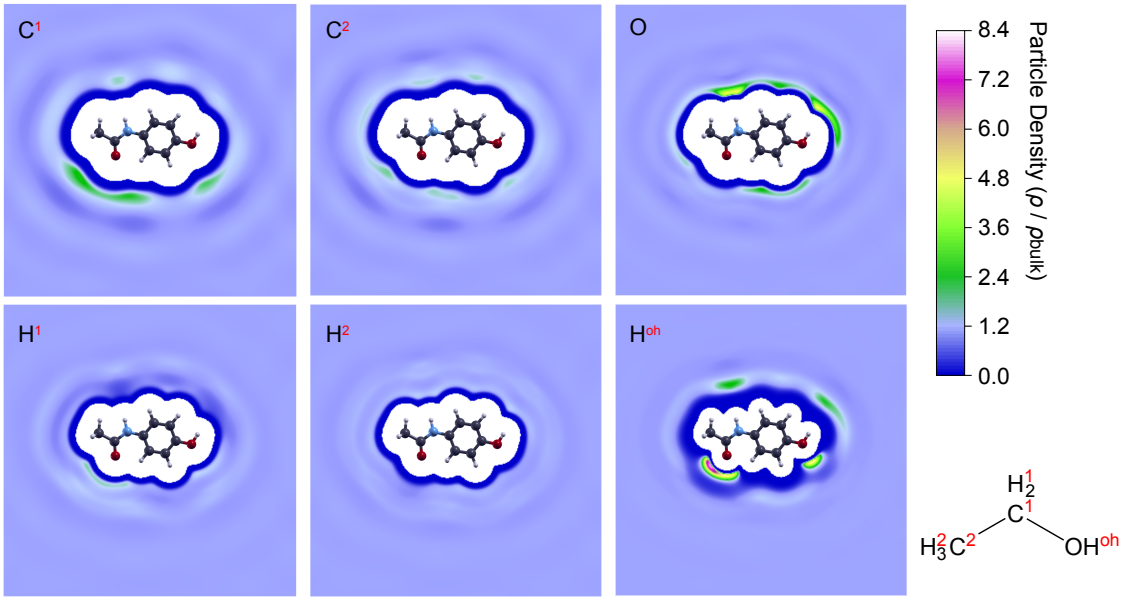

Fig. S3 Particle density distributions of ethanol around the solvated paracetamol molecule. Labels of corresponding atoms are marked in the inset.

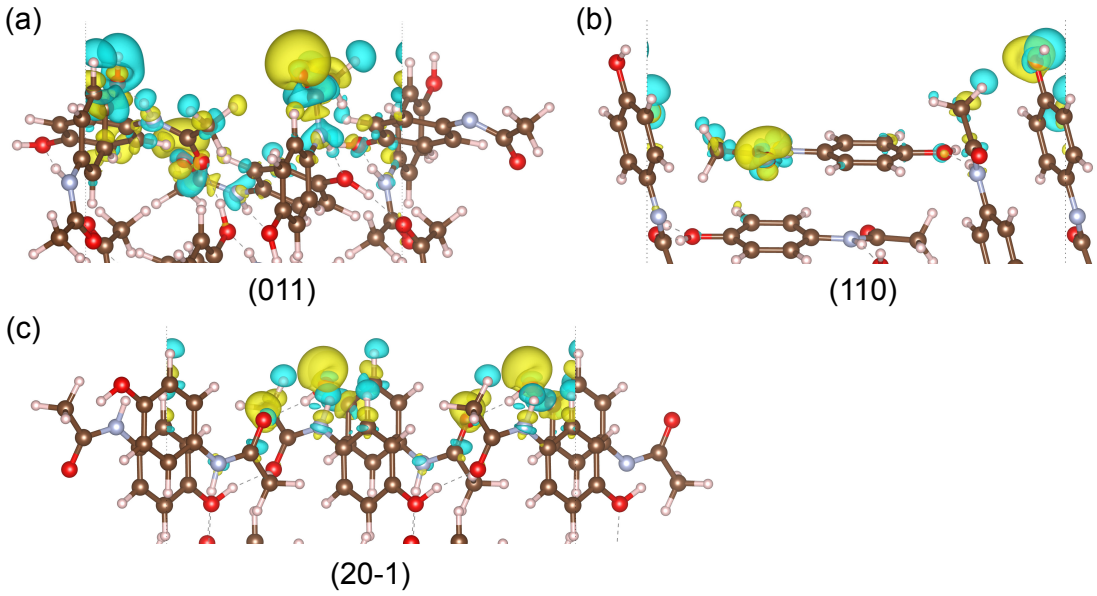

Fig. S4 Differences of charge density between solvated and non-solvated (a) (011), (b) (110) and (c) $(20\bar{1})$ surfaces (colour coded as **Fig. 2b**). The isosurface value is $\pm 3 \times 10^{-4}$ *e*.Bohr^{-3}.

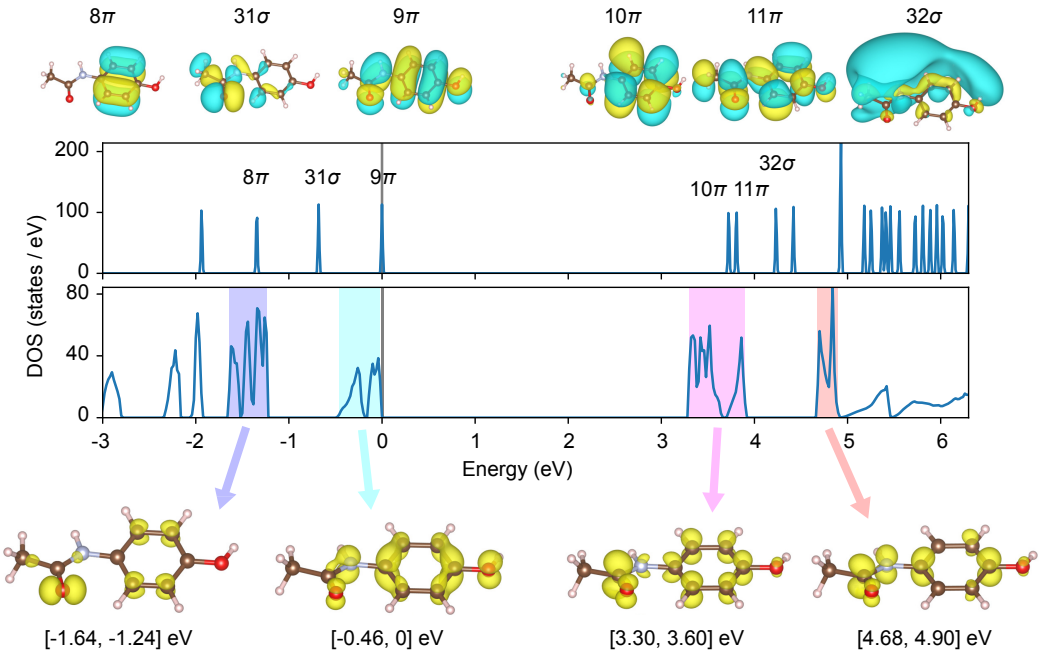

Fig. S5 (upper panel) MO and DOS of gaseous paracetamol. Types of MO are marked. (lower panel) DOS and ILDOS of Form I paracetamol crystal. Ranges of integration are marked. ILDOS of the non-equivalent molecule in crystal is displayed for clarity. Energy is aligned to the top of valence band.

In **Fig. S5**, both the valence band maximum (VBM) and the conduction band minimum (CBM) of the Form I crystal are π-type orbitals. The VBM corresponds to the 9π highest occupied molecular orbital (HOMO) of the gaseous paracetamol molecule, while the VBM-1 band shows mixed features of the 8π HOMO-2 and 31σ HOMO-1 orbitals. It is hard to distinguish the 10π lowest unoccupied molecular orbital (LUMO) and the 11π LUMO+1 orbital in the CBM and CBM+1 plots, so the hybridised LUMO and LUMO+1 orbitals are believed to generate those bands. **Fig. S5** illustrates that weak inter-molecular interactions have limited influences on molecular states, since the ILDOSs of crystal share similar shapes and energy rankings with the MOs of gaseous molecule[15].

Analysis of the (001) surface is included in the **Solvation of paracetamol surfaces** section of the manuscript. Notably, the integrated energy range is the VBM/CBM of surface layers, *i.e.*, the top two layers of molecules near the solid-liquid interface. As clearly shown in the total DOS of (001) surface, higher energy states exist beyond the VBM, which should be attributed to the bottom molecules exposed

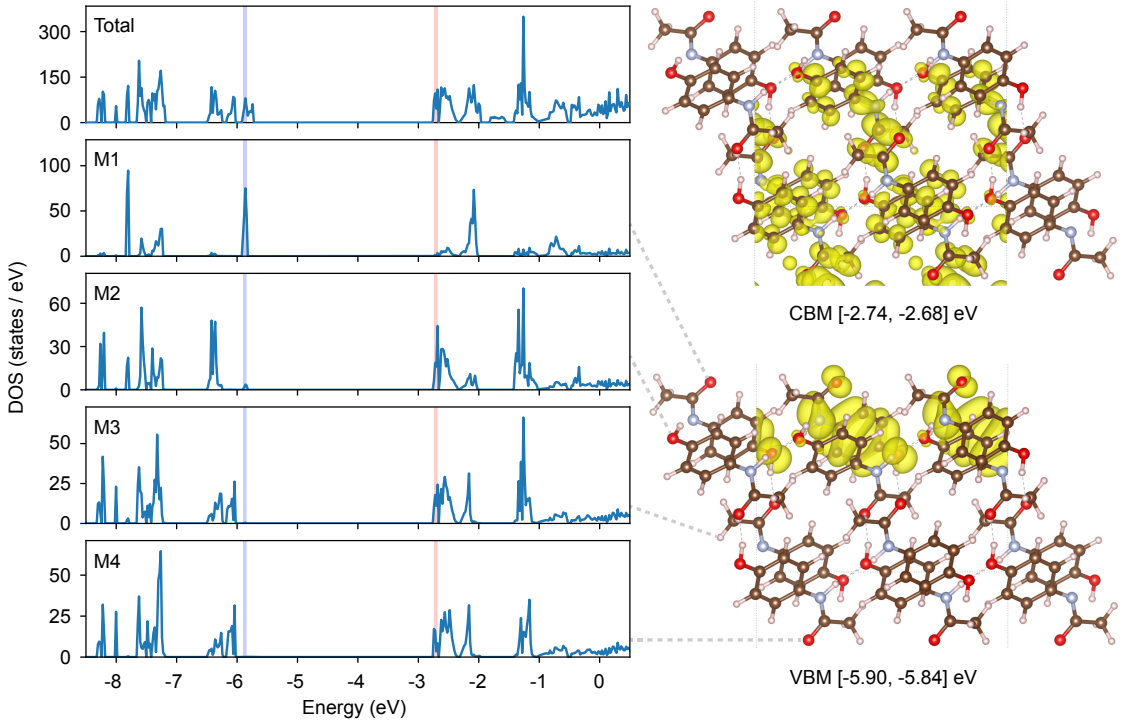

Fig. S6 (left) Total DOS and its projections onto the top two layers of molecules (M1-4) of the (001) surface. (right) ILDOS of VBM and CBM. Colour codes and legends are the same as **Fig. 4**.

to the vacuum layer. Since the right-hand 'vacuum-slab-solvent' ESM-RISM model is used, this is believed to be an artefact of the model. DOSs of M3 and M4 in the secondary layer show good agreement with that of Form I crystal (**Fig. S6**), so if an infinitely thick slab is used, DOSs of the lower lying molecules should converge to bulk DOS. The same artefact is also observed in the total DOSs of other surfaces (**Fig. 4; Fig. S7-S9**).

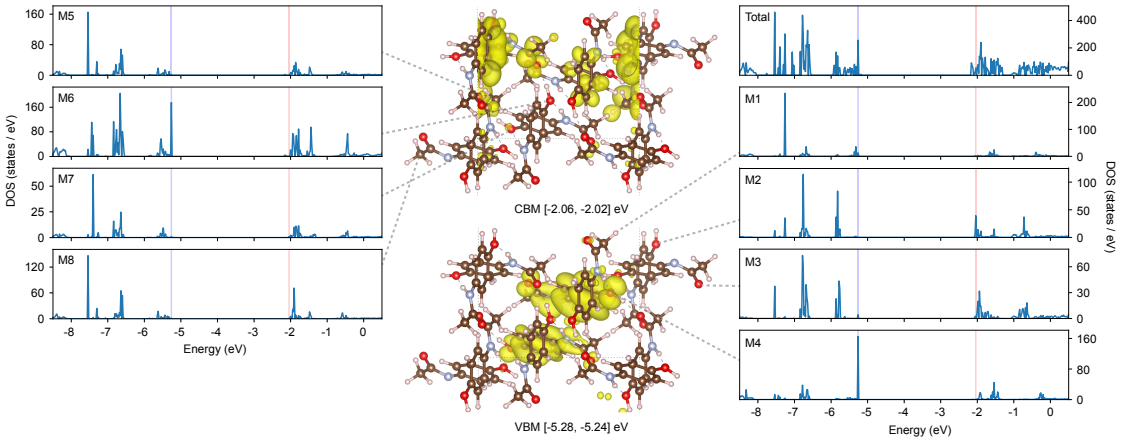

Fig. S7 (left) Total DOS and its projections onto the top two layers of molecules (M1-8) of the (011) surface. (right) ILDOS of VBM and CBM. Colour codes and legends are the same as **Fig. 4**.

Like the (010) surface, the solvent-induced charge redistribution takes place on the (011) surface (**Fig. S7**). Four nonequivalent molecules with distinct orientations exist on the (011) surface, increasing the complexity of surface geometry. M4 of the top layer contribute to VBM and accumulate charges locally due to the exposed acetyl O. However, only a moderate contribution to the VBM DOS of the higher M1 is observed. Though in the second layer, M6 also significantly contributes to VBM due to its closer distance to surface and to M4. Among the top-layer molecules, M2 and M3 contribute to the CBM, and the largest contribution is from the benzene ring of M2. As illustrated in **Fig. S4**, in general, charge depletes on the (011) surface, making M2 and M3, *i.e.*, the contributors to CBM, dominate the surface reactivity, probably due to the larger accessible areas of the amine and hydroxyl H atoms.

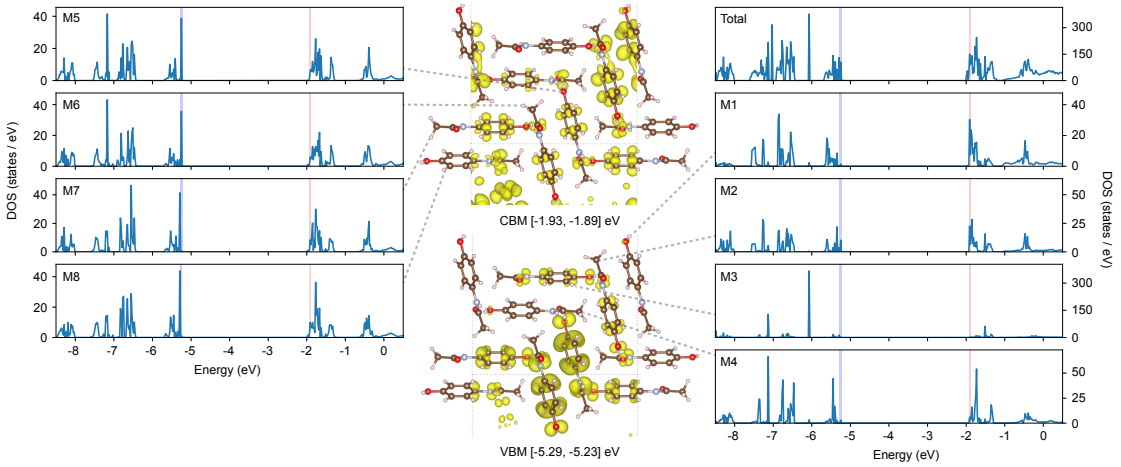

Fig. S8 (left) Total DOS and its projections onto the top two layers of molecules (M1-8) of the (110) surface. (right) ILDOS of VBM and CBM. Colour codes and legends are the same as **Fig. 4**.

For CBM of the (110) surface (**Fig. S8**), the most prominent contribution is from M1 and M2 of the upper layer, where the charge deficient hydroxyl H and benzene ring are exposed. The VBM/CBM of M3 shifts to higher energies, making it the most important contributor to surface VBM states. The exposed acetyl O of M3 might accumulate charges locally, while, overall, charge depletes on the (110) surface.

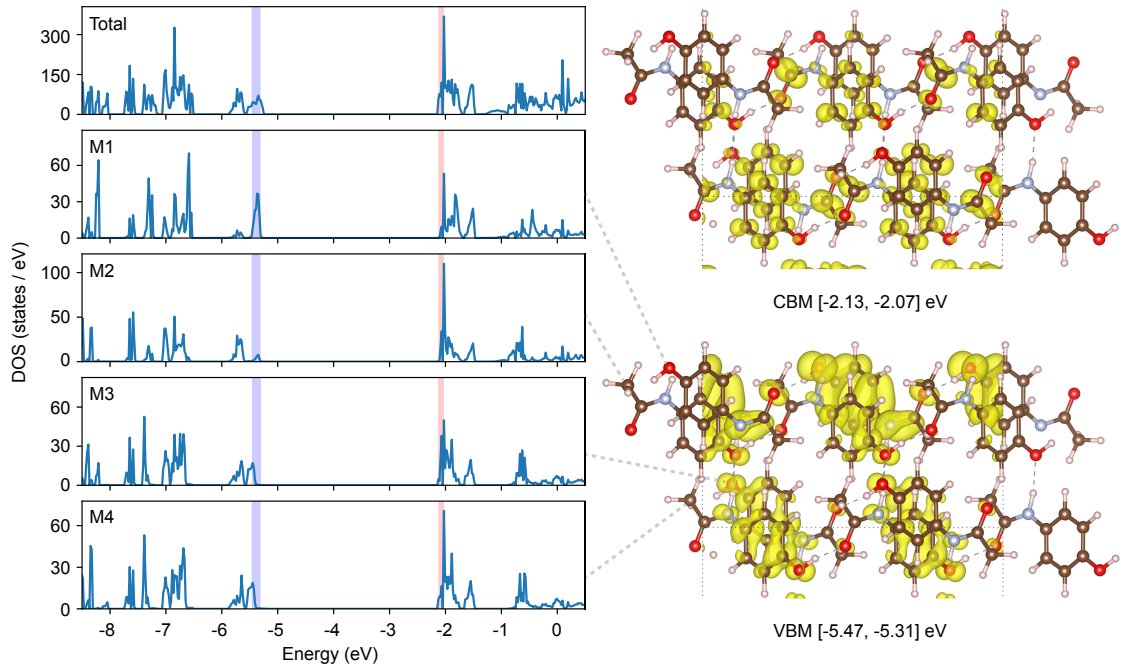

Fig. S9 (left) Total DOS and its projections onto the top two layers of molecules (M1-4) of the $(20\bar{1})$ surface. (right) ILDOS of VBM and CBM. Colour codes and legends are the same as **Fig. 4**.

Localised VBM/CBM states of the $(20\bar{1})$ surface are less prominent since the OH...O=C hydrogen bond is preserved (**Fig. S9**). Instead, the NH...OH hydrogen bond is broken, exposing the hydroxyl O of M1, which has weaker interactions with ethanol H^{oh} compared to the acetyl O. Therefore, the increased VBM DOS peak of M1 overlaps with the lower VBM DOS peaks of other molecules, indicating the limited solvation effect. The increased ILDOS of VBM is observed around M1, while M2 has the least contribution due to the electron affinitive amine H on the surface. Because of the limited solvation effect, the CBM energy range of $(20\bar{1})$ surface molecules is similar to that of bulk molecules. ILDOS of CBM shows the reduced contribution from M1 and the moderate increase in C of the acetyl C=O group of M2, which is also one of the charge deficient atoms of the solvated paracetamol molecule (**Fig. 2a**).

Analysis of the (001) surface (**Fig. S10a**) is included in the **Implicit adsorption** section of the manuscript. For the $(20\bar{1})$ surface (**Fig.**

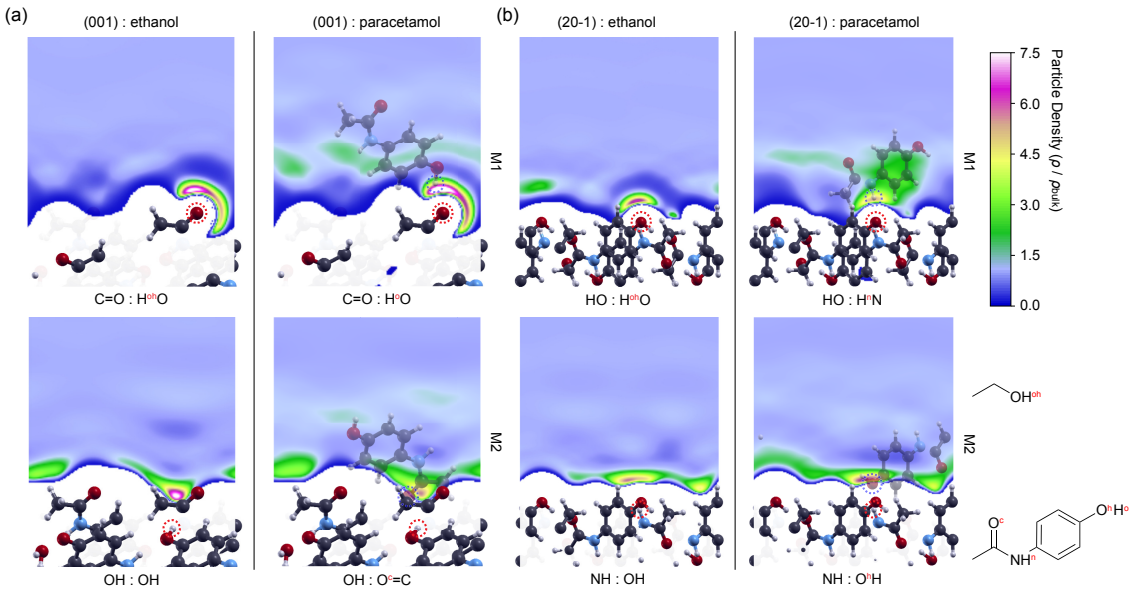

Fig. S10 Particle distributions of implicit ethanol and paracetamol near (a) (001) and (b) $(20\bar{1})$ surfaces. All the annotations are consistent with **Fig. 5**. Labels of molecule (M1 and M2) right to the figures denote the orientations of adsorbate, which are consistent with **Fig. S6** and **Fig. S9**.

S10b), the ethanol H^{oh} has the highest accumulation on the surface, which simultaneously increases steric hindrances to M1 and M2. A large reduction of $\rho(H^n)$ is observed as the ethanol H^{oh} binds directly to its adsorption site (hydroxyl O) and screens it. In comparison, the distributions of $\rho(O)$ of ethanol and $\rho(O^h)$ of M2 are more uniform, probably due to the lower adsorption site (amine H) whose interactions with the solvent are limited by the reduced solvent accessible area.

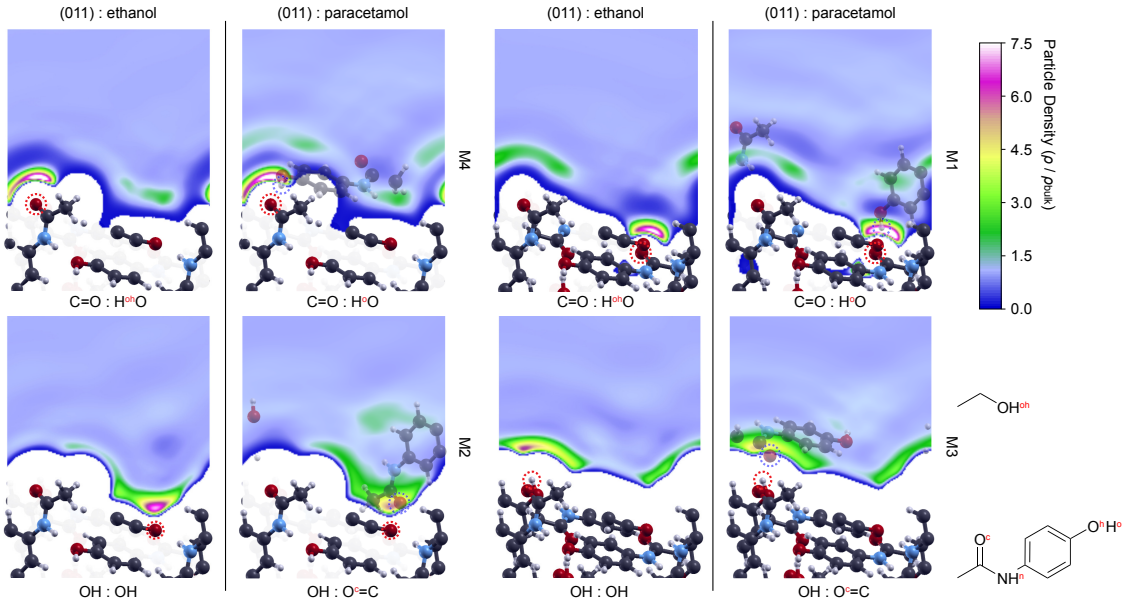

Fig. S11 Particle distributions of implicit ethanol and paracetamol near the (011) surface. All the annotations are consistent with **Fig. 5**. Labels of molecule (M1-4) right to the figures denote the orientations of adsorbate, which are consistent with **Fig. S7**.

The significant increase of $\rho(H^o)$ around acetyl O indicates fast adsorptions of M1 and M4 (**Fig. S11**). In comparison, $\rho(O)$ of ethanol is more prominent than $\rho(O^c)$ of paracetamol, reducing near-surface densities of M3 and M4. This is similar to the case of the (001) surface, indicating that a similar adsorption mechanism probably exists on the (011) surface. Besides, the highest lying M1 brings non-negligible steric hindrances to all adsorbates. The orientation of M2 reduces hindrances it encounters, since it is almost parallel to M1, while M3 might experience the stronger hindrance due to its nearly perpendicular orientation to M1, which explains its lowest near-surface density.

The four broken hydrogen bonds on the (110) surface are connected to M2 and M4 (**Fig. S12**). Strong accumulations of ethanol H^{oh}

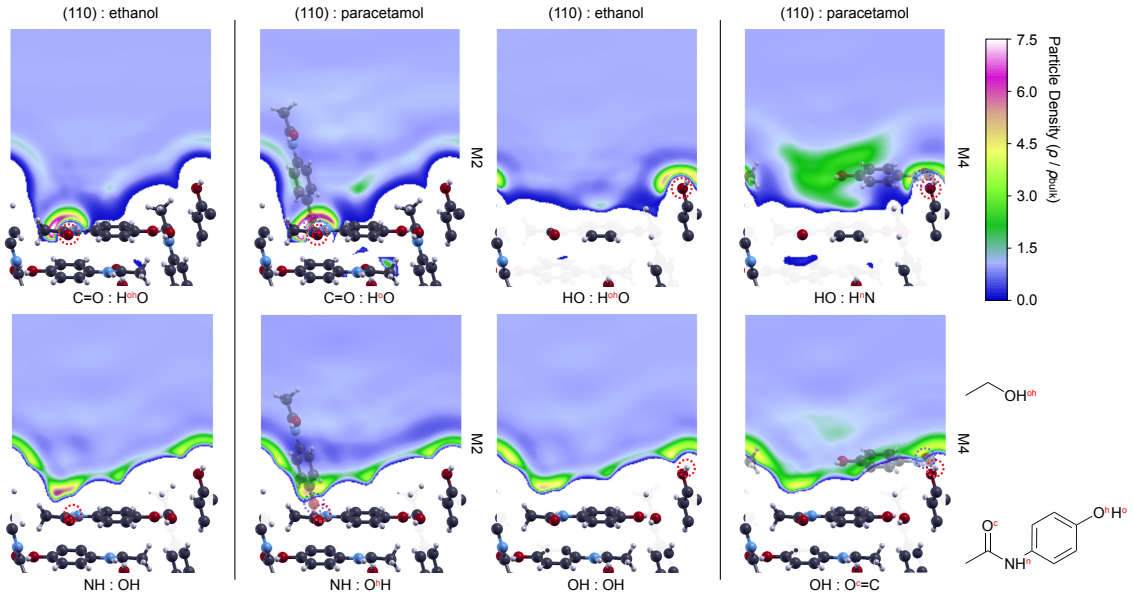

Fig. S12 Particle distributions of implicit ethanol and paracetamol near the (110) surface. All the annotations are consistent with **Fig. 5**. Labels of molecule (M2 and M4) right to the figures denote the orientations of adsorbate, which are consistent with **Fig. S8**.

and paracetamol H^o are observed around the acetyl O. In comparison, $\rho(H^n)$ is much less accumulated than $\rho(H^o)$ due to the weaker NH...OH hydrogen bond. Instead, a stronger $\rho(H^{oh})$ of ethanol is observed, suggesting that the paracetamol-ethanol interactions overtake the paracetamol-paracetamol interactions in the presence of unsaturated NH...OH hydrogen bonds, which is consistent with the observations of the $(20\bar{1})$ surface. The distributions of $\rho(O^h)$ and $\rho(O^c)$ are scattered similarly around the hydroxyl and amine H atoms, which exhibit patterns different from the hydrogen atoms. This mismatch probably indicates the misorientation of near-surface adsorbates, where an orientation different from either M2 and M4 might be adopted, but the energy-minimum orientation is so far unclear.

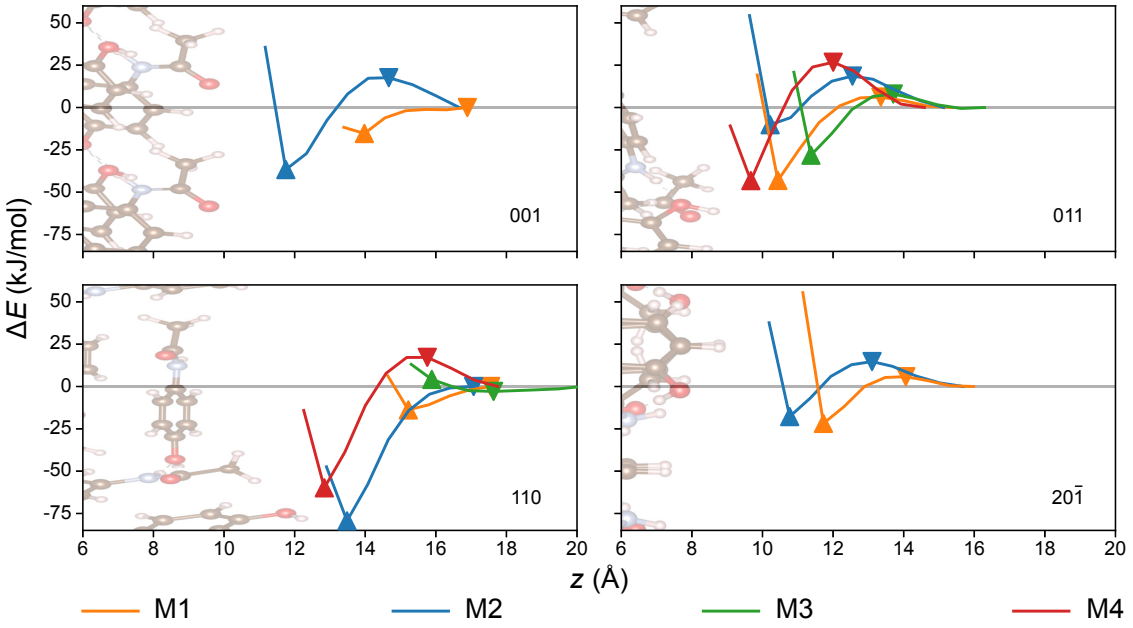

Fig. S13 The adsorption energy profiles onto (001), (011), (110) and $(20\bar{1})$ surfaces. Labels of molecules are consistent with **Fig. S6**-**S9**. The z coordinate of molecular mass centre is used to indicate the position of adsorbate. The equilibrium positions of molecules are indicated by the up triangles.

The scanned adsorption energy profiles (ΔE) of the (001), (011), (110) and $(20\bar{1})$ surfaces are illustrated in **Fig. S13**. The drops in ΔE near all surfaces are not noticeably different from those near the (010) surface, again suggesting that its fast regrowth is not controlled by thermodynamic factors. A difference in ΔE of 21.30 kJ/mol is observed between the equilibrium M1 and M2 on the (001) surface,

while ΔE of the equilibrium M2 and M4 on the (110) surface differ by 19.52 kJ/mol, both of which could selectively attract adsorbates with specific orientations. On the (110) surface, the equilibrium ΔE of M2 and M4 are significantly lower than those of M1 and M3 due to the hydrogen bond formation. M2 also exhibits the lower energy barrier in the diffusion path, which promotes the adsorption of M2 and increases the steric hindrance of M4. Similar equilibrium ΔE between differently orientated adsorbates on the (011) and (20$\bar{1}$) surfaces are reported, increasing the rotational freedom of the adsorbate near these surfaces, which might enhance steric hindrances for adsorbates with the desired orientations.

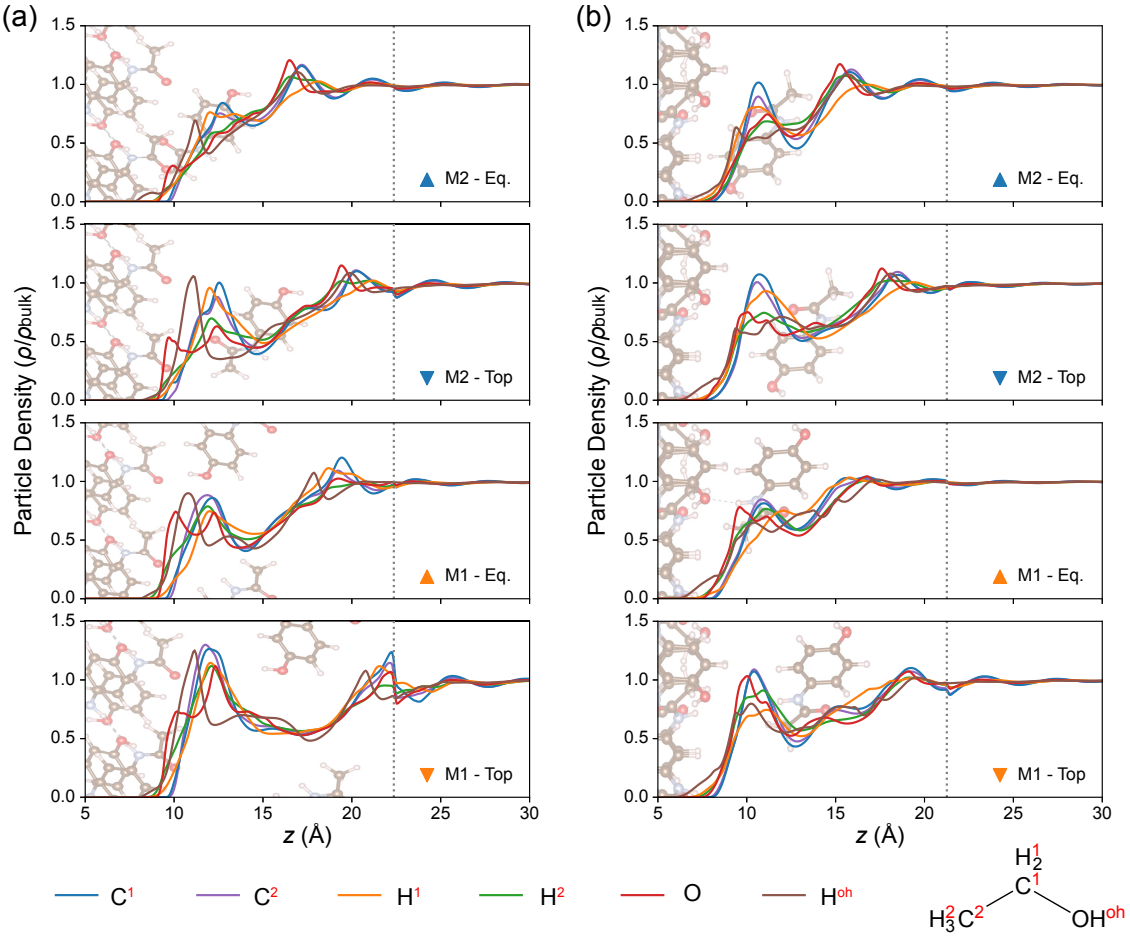

Fig. S14 Plan-averaged solvent particle density distributions of the ethanol solvent during the paracetamol adsorption onto (a) (001) and (b) (20$\bar{1}$) surfaces. All the annotations are consistent with **Fig. 6** Labels of molecules are consistent with **Fig. S6** and **Fig. S9**.

Although similar ΔE profiles to those of the (010) surface (**Fig. 6a**) are reported for the (001) surface, non-negligible differences in the near-surface solvent structure are revealed (**Fig. S14a**). Ethanol accumulates prominently between the adsorbate and the (001) surface when the adsorbate is located at the top of barrier, limiting its diffusion rate and reducing the surface growth. In both cases, ethanol H^{oh} accumulates closer to the surface due to its strong interaction with acetyl O on the (001) surface. The peaks of ethanol C^1, C^2 and O are farther from the surface due to the ordering of solvent structure. At equilibrium adsorption sites, the density of the intermediate ethanol layer is reduced, but there are still observable peaks of $\rho(H^{oh})$, indicating that the whole adsorption process on the (001) surface is strongly influenced by the competition between paracetamol and ethanol. In addition, the large reduction in near-surface ethanol densities during the adsorption of both M1 and M2 probably requires additional energy to lower and overcome these barriers. Compared to the particle density distributions near the (010) surface (**Fig. 6**), this observation might be helpful in evaluating the competition between ethanol and paracetamol and explaining the surface growth dominated by unsaturated hydrogen bonds.

Similarly, ethanol layers between the adsorbate and the (20$\bar{1}$) surface are identified throughout the adsorption process, increasing the competition between paracetamol and ethanol and limiting the growth rate of the surface. Compared to the case of (001) surface, the reduction in near-surface ethanol density is less obvious when the lower M2 reaches the equilibrium position, while a slightly larger but comparable reduction for M1 is noticed. The similar adsorption processes of M1 and M2 reduce the orientation selectivity, increasing the rotational freedom of the paracetamol adsorbates.

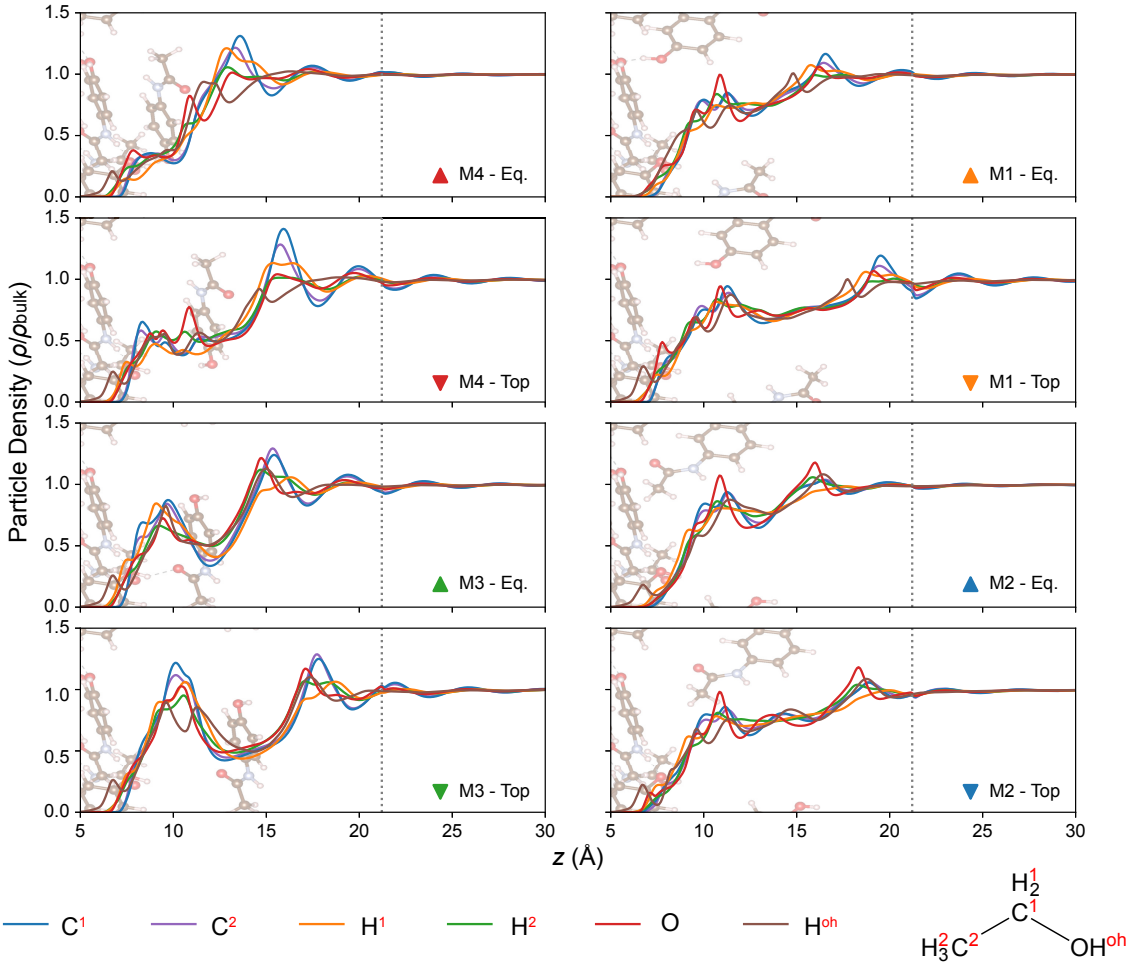

Fig. S15 Plan-averaged solvent particle density distributions of the ethanol solvent during the paracetamol adsorption onto the (011) surface. All the annotations are consistent with **Fig. 6**. Labels of molecules are consistent with **Fig. S7**.

In all cases, ethanol accumulation regions are observed between the (011) surface and the adsorbates (**Fig. S15**), indicating the strong surface-solvent interactions. For M1, M3, and M4, the near-surface ethanol densities are reduced during adsorption, as a result of hydrogen bond formation. Though in principle, an OH...O=C bond is formed between M2 and the surface, the hydroxyl H on the (011) surface is rotated to the bulk after structural relaxation of the slab model. Therefore, the adsorption of M2 probably requires additional energy to rotate the hydroxyl group on the surface, which is not captured in this study due to the fixed surface geometry.

Distinct solvent structures are revealed for the differently orientated adsorbates on the (110) surface, as illustrated in **Fig. S16**. M3 and M4 are almost parallel to the (110) surface, significantly increasing their contact area with the intermediate ethanol layer. In contrast, M1 and M2 adopt a nearly vertical orientation, which reduces contact and limits interactions with the layer, prominently lowering the barrier on the diffusion path.

On the other aspect, the larger equilibrium ΔE of M2 and M4 can be explained by the hydrogen bond formation with surface molecules, while for M1 and M3, ΔE is much smaller, since no hydrogen bonds are formed. Therefore, it can be estimated that M2 and M4 will be adsorbed first to form hydrogen bonds with M1 and M3 in the following step. However, the different orientations of M2 and M4 lead to distinct adsorption kinetics. A large drop in particle densities is noticed during the adsorption of M4, indicating that a larger energy is probably essential to remove the near-surface solvent layer, which reduces its adsorption rate. With M2 adsorbed at a higher rate, its unsaturated hydrogen bonds might promote the sequential adsorption of M3, which adopts a similar orientation as M4, increasing competitions and steric hindrances near the surface. Consequently, the adsorption rate of M4 is further reduced. Besides, on the (110) surface, the adsorption site of M3 largely overlaps with that of M4, where vacancies in the lattice might be introduced if M3 is adsorbed prior to M4. This finding offers a probable explanation for the experimentally observed morphological instability and the high defect concentration of the (110) surface[14], which originates from the synergy of its unique surface geometry and the orientation-dependent adsorption kinetics of paracetamol adsorbates.

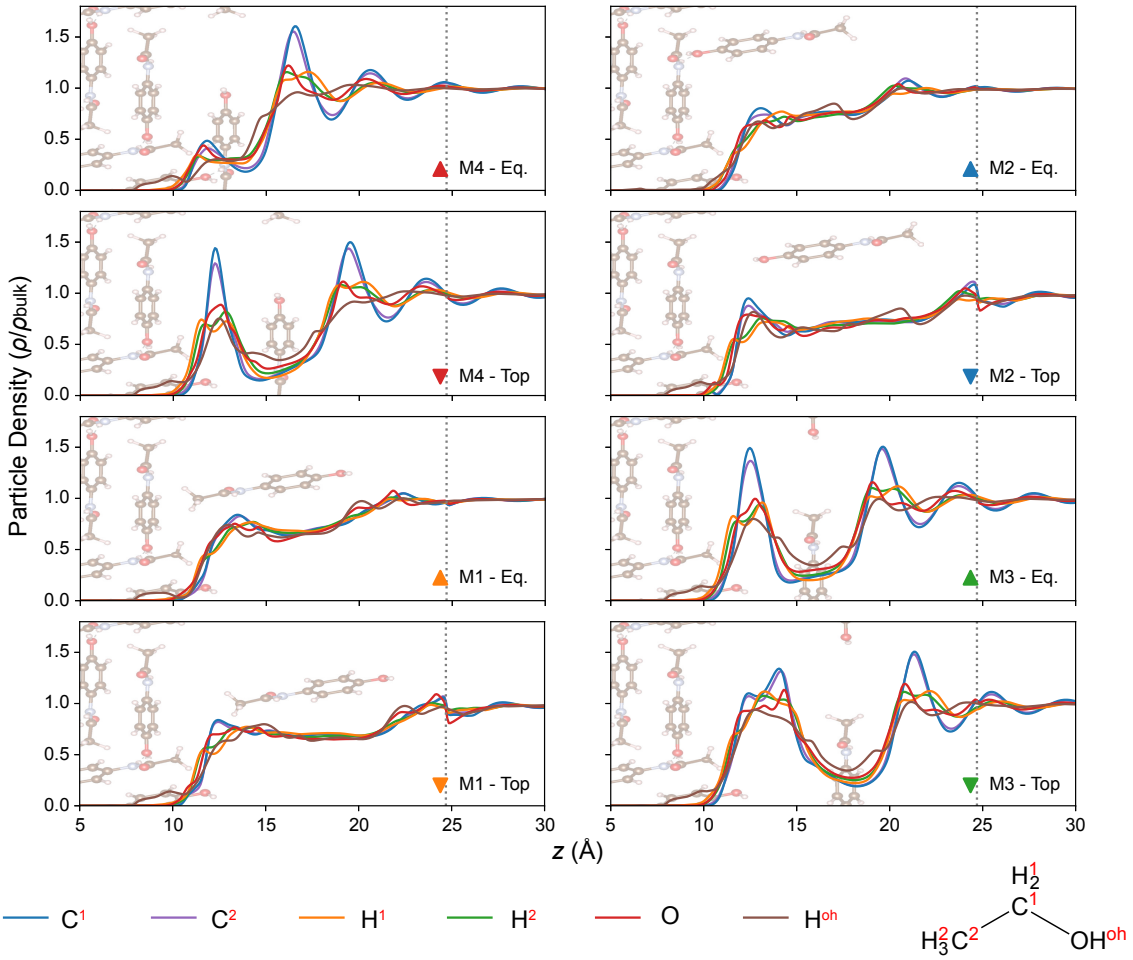

Fig. S16 Plan-averaged solvent particle density distributions of the ethanol solvent during the paracetamol adsorption onto the (110) surface. All the annotations are consistent with **Fig. 6**. Labels of molecules are consistent with **Fig. S8**.

References

1 P. Giannozzi, S. Baroni, N. Bonini, M. Calandra, R. Car, C. Cavazzoni, D. Ceresoli, G. L. Chiarotti, M. Cococcioni, I. Dabo, A. D. Corso, S. d. Gironcoli, S. Fabris, G. Fratesi, R. Gebauer, U. Gerstmann, C. Gougoussis, A. Kokalj, M. Lazzeri, L. Martin-Samos, N. Marzari, F. Mauri, R. Mazzarello, S. Paolini, A. Pasquarello, L. Paulatto, C. Sbraccia, S. Scandolo, G. Sclauzero, A. P. Seitsonen, A. Smogunov, P. Umari and R. M. Wentzcovitch, *Journal of Physics: Condensed Matter*, 2009, **21**, 395502.

2 P. Giannozzi, O. Andreussi, T. Brumme, O. Bunau, M. B. Nardelli, M. Calandra, R. Car, C. Cavazzoni, D. Ceresoli, M. Cococcioni, N. Colonna, I. Carnimeo, A. D. Corso, S. d. Gironcoli, P. Delugas, R. A. DiStasio, A. Ferretti, A. Floris, G. Fratesi, G. Fugallo, R. Gebauer, U. Gerstmann, F. Giustino, T. Gorni, J. Jia, M. Kawamura, H.-Y. Ko, A. Kokalj, E. Küçükbenli, M. Lazzeri, M. Marsili, N. Marzari, F. Mauri, N. L. Nguyen, H.-V. Nguyen, A. Otero-de-la Roza, L. Paulatto, S. Poncé, D. Rocca, R. Sabatini, B. Santra, M. Schlipf, A. P. Seitsonen, A. Smogunov, I. Timrov, T. Thonhauser, P. Umari, N. Vast, X. Wu and S. Baroni, *Journal of Physics: Condensed Matter*, 2017, **29**, 465901.

3 R. Dovesi, V. Saunders, C. Roetti, R. Orlando, C. Zicovich-Wilson, F. Pascale, B. Civalleri, K. Doll, N. Harrison, I. Bush, P. D'Arco, M. Llunell, M. Causà, Y. Noël, L. Maschio, A. Erba, M. Rérat, S. Casassa, B. Searle and J. Desmarais, *Gruppo di Chimica Teorica, Dipartimento di Chimica, Università di Torino*, 2023.

4 C. McLoughlin, W. McMinn and T. Magee, *Powder Technology*, 2003, **134**, 40–51.

5 W. L. Jorgensen and J. Tirado-Rives, *Journal of the American Chemical Society*, 1988, **110**, 1657–1666.

6 S. Nishihara, *nisihara1/MOLs*, 2023, `https://github.com/nisihara1/MOLs`.

7 S. Nishihara and M. Otani, *Physical Review B*, 2017, **96**, 115429.

8 D. K. Owens and R. C. Wendt, *Journal of Applied Polymer Science*, 1969, **13**, 1741–1747.

9 J. Y. Y. Heng, F. Thielmann and D. R. Williams, *Pharmaceutical Research*, 2006, **23**, 1918–1927.

10 O. Myronyuk, D. Baklan, A. M. Rodin, E. Vanagas and Z. Yong, *Coatings*, 2023, **13**, 1104.

11 J. Y. Y. Heng, A. Bismarck, A. F. Lee, K. Wilson and D. R. Williams, *Langmuir*, 2006, **22**, 2760–2769.

12 J. Y. Y. Heng and D. R. Williams, *Langmuir*, 2006, **22**, 6905–6909.

13 J. Panzer, *Journal of Colloid and Interface Science*, 1973, **44**, 142–161.

14 R. I. Ristic, S. Finnie, D. B. Sheen and J. N. Sherwood, *The Journal of Physical Chemistry B*, 2001, **105**, 9057–9066.

15 N. Kovačević and A. Kokalj, *The Journal of Physical Chemistry C*, 2011, **115**, 24189–24197.